



Reveal the relation between spatial patterns of rainfall return levels and landslide density

Slim Mtibaa¹, Haruka Tsunetaka¹

¹Department of Disaster Prevention, Meteorology and Hydrology, Forestry and Forest Products Research Institute,
5 Tsukuba city, 305-8687, Japan

Correspondence to: Slim Mtibaa (mtibaaslim@ffpri.affrc.go.jp)

Abstract. It is known that the spatial rainfall pattern can mark landslide distribution across the landscape during extreme triggering events. However, the current knowledge of rainfall controls on this distribution remains limited. Here, to reveal what rainfall characteristics control landslide spatial distribution, we explore the spatiotemporal pattern of a rainfall event that triggered over 7,500 landslides (area $\approx 10^0\text{--}10^4\text{ m}^2$) at a regional scale with an area of $\approx 400\text{ km}^2$ in Japan. Using a 5-km resolution radar-driven hourly precipitation dataset with 32 years of records, we compared rainfall return levels for various time range from 1 to 72 h and landslide density in each $\approx 25\text{ km}^2$ grid cell. The results show that, even if the surface slope distribution within grid cells is similar, the number of landslides in a $\approx 25\text{ km}^2$ grid cell was substantially high when the rainfall return levels exceeded the 100-year return period in all examined timespans (i.e., 1–72 h). In contrast, when only specific-duration rainfall intensities (e.g., 6–48 h) exceeded the 100-year return level, the landslide density in corresponding grid cells tended to be low. Consequently, the landslide density increased with the increase in the rainfall return level of various timespans rather than a specific rainfall intensity, such as downpours for a few hours or long-term cumulative rainfall for 48 h. Moreover, with the increase in the landslide density, the number of relatively large landslides exceeding $\approx 400\text{ m}^2$ increased. Therefore, the spatial differences in rainfall return levels potentially constrain the density of total landsliding and relatively large landslides. In this sense, whether rainfall intensities reach high return levels rarely experienced in a wide timespan ranging from a few hours to several days is one of the key determinants of the spatial distribution of landslides and the extent of related hazards.

1 Introduction

Landslides are natural geomorphic processes driving long-term landscape evolution (Korup et al., 2010), which may impose substantial changes in hillslope and fluvial systems and significant human and economic losses (Froude and Petley, 2018; Jones et al., 2021). Rainfall is the most common trigger of landslides (Sidle and Bogaard, 2016). Although rainfall may provoke individual landslides with localized impacts, large-scale extreme and intense rainfall events often induce numerous landslides widely spread over the landscape (Emberson et al., 2022). In such cases, the impacts span the



spatial extent of the triggering event, and their significance depends on the location, number, and size of triggered
30 landslides (Medwedeff et al., 2020; Milledge et al., 2014; Benda and Dunne, 1997). Therefore, revealing rainfall controls
on landslide spatial distribution is fundamental for assessing landscape changes and supporting hazard prediction efforts.
Current knowledge on how rainfall controls spatial distribution and characteristics of landslides remains limited and
difficult to constrain. A direct cause-effect link between rainfall and landslide occurrence does not exist because the
landsliding mechanism is also governed by slope material properties (e.g., strength, soil depth, hydraulic conductivity)
35 (Berti et al., 2012). Accordingly, landslide occurrence timing and geometric features (e.g., area, volume, and depth) differ
within the catchment (Yamada et al., 2012; Yano et al., 2019; Guzzetti et al., 2004) and hillslope scales (Büschelberger et
al., 2022) due to disparate hydromechanical responses of slopes to forcing rainfall. This suggests that the effective
rainfall period that favors landsliding, which typically includes the rainfall that prepares hillslopes for failure “cause” and
the one that lastly pushes slopes to slide “trigger” (Bogaard and Greco, 2018), is variable and hard to constrain. Physical
40 process-based models can solve this problem by computing how rainfall exerts pore pressure variations that affect slope
stability and predict landslide locations (e.g., Wu and Sidle, 1995; Iverson, 2000; Lanni et al., 2012) and sizes (e.g.,
Milledge et al., 2014). However, in practice, their application and calibration are often hindered by difficulties in
collecting detailed input parameters (i.e., slope material properties) (Bogaard and Greco, 2018).

In light of these problems, exploring spatial relationships between landslide distribution, often described as density (e.g.,
45 number/km² or area/km²), and the characteristics of triggering events, deemed critical in the landsliding mechanism,
emerges as an alternative empirical approach. Existing studies attempted to constrain these quantitative correlations by
relying on a catalog of individual landslide information (e.g., Gao et al., 2018) or detailed landslide inventories triggered
by a single or multiple rainfall events (e.g., Marc et al., 2018; Chang et al., 2008). So far, we lack information on the best
rainfall attribute(s) that characterize triggering rainfall conditions. Some studies showed increased landslide density with
50 increased cumulative rainfall amount, event duration, average rainfall intensity, the maximum amount for short durations
(e.g., 1, 3, 4, 24 h), or antecedent rainfall (Marc et al., 2018; Chen et al., 2013; Chang et al., 2008; Dai and Lee, 2001;
Abancó et al., 2020). Other works relied on the theory of landscape coevolution with local climate (Benda and Dunne,
1997; Iida, 1999) and demonstrated that normalized rainfall metrics by the mean annual precipitation (Ko and Lo, 2016)
or the 10-year return period rainfall amount (Marc et al., 2019) are better predictors for landsliding. These empirical
55 relationships provided insights into rainfall controls on landslide spatial distribution. However, it often linked specific
rainfall attributes such as the maximum rainfall amount for 48 h to landslide density, which leads to overlooking the
potential control of temporal rainfall pattern (i.e., repeated fluctuations of rainfall intensity within the rainfall event)
characteristics on landslide density.

Analyzing the temporal rainfall pattern using multiple timespans would characterize landslide-triggering rainfall by
60 disparate measures, in terms of duration and intensity, rather than a specific rainfall metric (e.g., total rainfall amount, the
maximum rainfall amount for 48 h). Therefore, it can consider the different possible rainfall periods responsible for



triggering landslides from short to long duration. Note that high rainfall return level (i.e., recurrence interval) can be a proxy of the critical conditions causing landslides (Iida, 2004; Griffiths et al., 2009; Segoni et al., 2014, 2015). Given this, focusing on an extreme rainfall event that triggered over 7,500 landslides in an area of around 400 km² in the northern part of the Kyushu region in southern Japan, we investigated whether spatial patterns of rainfall return levels govern landslide density. Using a gridded rainfall dataset with a ≈ 5 -km resolution, we compared rainfall return level for various time range from 1 to 72 h and landslide density in each ≈ 25 -km² grid cell to investigate whether the landslide density increase in grid cells where rainfall intensities reach high return levels that are rarely experienced. The present research is expected to provide insights into what rainfall characteristics control landslide spatial distribution and when rainfall may cause high landslide density. Thus, it can have promising implications for supporting hazard prediction efforts and understanding landscape evolution.

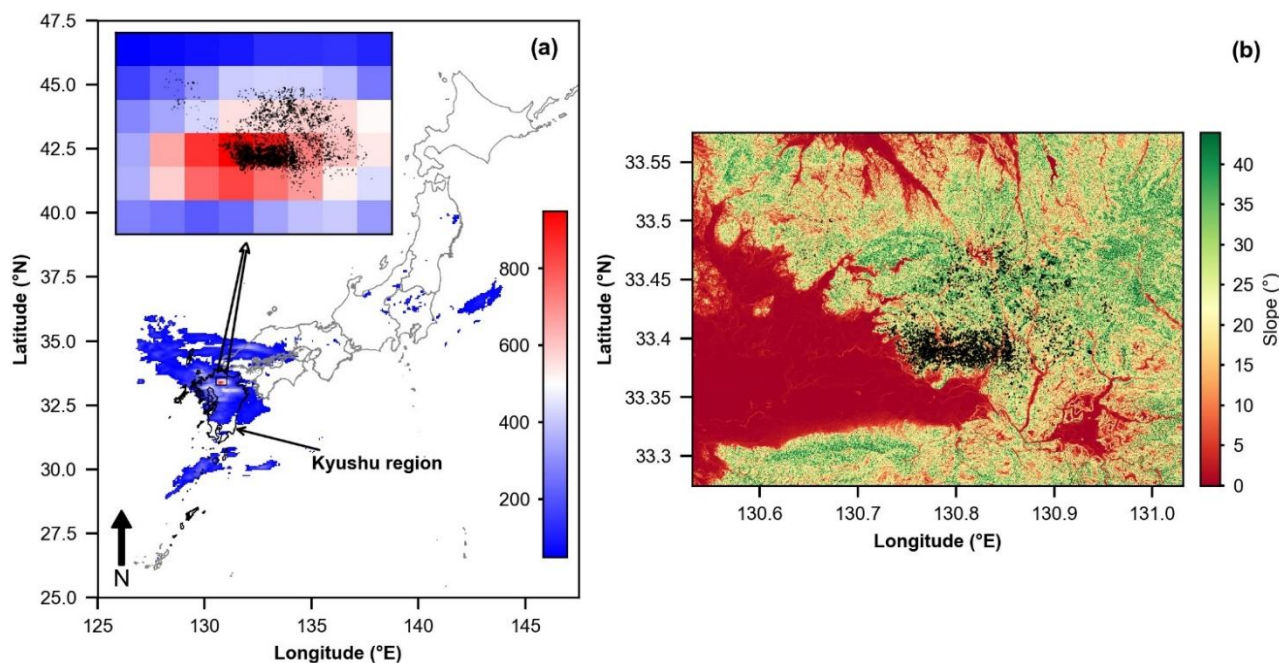
2 Material and Methods

2.1 Study site and landslide characteristics

The study focuses on an area of around 400 km² in the northern part of the Kyushu region in southern Japan (Fig. 1a). The examined area experienced an extreme rainfall event on July 5 and 6, 2017, caused by a linear mesoscale convective system (Hirockawa et al., 2020), that triggered over 7,500 landslides (Fig. 1a).

If the landslides occurred in a homogeneous regolith, which reduces the likelihood of their link to complex geotechnical site characteristics (Marc et al., 2019), the interpretation of the potential rainfall controls on landslide occurrence would be possible. Indeed, most landslides triggered by the examined rainfall event occurred on forested hillslopes with similar lithological settings (granodiorite and pelitic schist) but disparate density and geomorphic features (Chigira et al., 2018). Moreover, most landslides were shallow and affected mainly the soil mantle. Thus, the examined area provided an adequate test field to investigate relationships between rainfall return levels and landslide density because at least the land cover and lithological settings of the hillslopes can be deemed relatively homogenous.

Our research relied on the landslide inventory prepared by the Ministry of Land, Infrastructure, Transport, and Tourism of Japan from orthophotos of 0.1-m resolution and digital elevation models (DEM) of 1-m resolution acquired by Airborne Laser Scanning in July 2017 (i.e., immediately after the landslide occurrence). The mapping method of landslide scars involves three steps. The first step identifies bare land hillslopes as landslides and delineates them manually from the orthophotos. The second step rectifies the delineated landslide scars using DEM data acquired after the disaster and maps them as polygons. The third step compares these polygons to satellite and aerial images dated before July 2017 to exclude landslides that formerly occurred in the region. The inventory counts 7,676 polygons identifying widespread landslides in the examined area (Fig. 1b). These polygons represent only landslide source areas (scars) and omit runout zones.



95 **Figure 1: (a) Cumulative rainfall for 5 and 6 July 2017 (> 50 mm) and location of triggered landslides (black polygons in the inset figure). (b) Distribution of the landslides (black polygons) over the Slope map of the affected region.**

Size characteristics of the landslides were investigated by examining the frequency-area distribution (FAD), which plots landslide sizes (i.e., measures of the area) with corresponding frequencies (Malamud et al., 2004). The FAD can determine whether the landslide inventory follows the fundamental property of landslides (Hovius et al., 1997). For the landslide inventory this study relied on, the FAD exhibited a rollover (i.e., the peak point of the distribution) at around 100 10² m², below which the frequency of small landslides decreases, and a cutoff point of 439 m² (Fig. 2), which was derived using the method of Clauset et al., (2009). The frequency distribution of landslides with area size exceeding the cutoff (area > 439 m²), which accounted for 28.12 % of the total inventory and referred to, hereafter, as medium and large landslides, fitted a power-law function with the scaling parameter (β) of 2.26. This exponent is within the typical range of 2–3 derived by other landslide inventories (e.g., Guzzetti et al., 2002; Marc et al., 2018) and suggests that small 105 landslides were more frequent than medium and large landslides (area > cutoff point of 439 m²) during the studied event. Accordingly, it is important to note that the landslide inventory follows the fundamental properties of landslides, as the FAD can fit an inverse gamma distribution with a right tail that decays as a power law (Stark and Hovius, 2001). Considering the high resolution of DEM and orthophotos used for constructing the examined landslide inventory, which is significantly lower than the cutoff point and allowed capturing the geometric features of landslides with size in the 110 order of 0.02 m², it is evident that the observed divergence was due to physical processes rather than under-sampling of small landslides (Frattini and Crosta, 2013; Medwedeff et al., 2020).

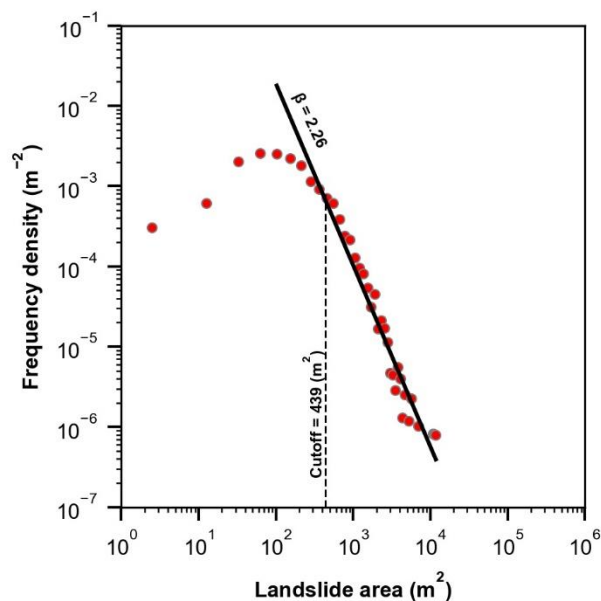


Figure 2: Non-cumulative frequency area distribution of the landslide inventory.

115 Additionally, we quantified landslide angles as the median slope at landslide scars derived from the analysis of a 10-m
resolution DEM, which was developed by the Geospatial Information Authority of Japan (GSI) from 1:25,000-scale
topographic maps dated before the disaster (Fig. 1b). For landslides with an area smaller than 100 m² (i.e., DEM pixel
size), the slope value of the pixel was taken as landslide angle. The landslide angles ranged between 0.45° and 51.03°
(median = 27.20°). More than 90 % of the triggered landslides were associated with hillslopes of more than 16.26° slope
(Supporting information, Fig. S1). This latter was used as a threshold angle for calculating metrics of landslide density.

120 2.2 Rainfall data and processing methods

We employed the radar/rain gauge analyzed (R/A) precipitation dataset (1988–2019) to examine the spatiotemporal
pattern of the triggering rainfall and derive the return levels of rainfall intensities for multiple timespans in the Intensity
Duration Frequency (IDF) curves. The R/A datasets are developed by the Japan Meteorological Agency (JMA) from
reflected echo intensities and doppler velocities of 46 C-band radars and adjusted to rainfall measurements obtained from
125 local rain gauges (Makihara, 2000; Nagata, 2011). This product provides hourly adjusted rainfall estimates with a spatial
resolution of ≈ 5 km (1988–2001), ≈ 2.5 km (2002–2005), and ≈ 1 km (from 2006) (Mtibaa and Asano, 2022). Therefore,
for homogeneity reasons, we downscaled the data from 2002 to ≈ 5 km spatial resolution (same as the resolution of the
1988–2001 dataset) using the method recommended by Nagata and Tsujimura (2006). We selected this method because it
produced homogenous maximum daily rainfall time series based on the homogeneity tests applied by Urita et al. (2011).



130 It spatially averages the 1 km product to 2.5 km spatial resolution and downscales the 2.5 km product to 5 km spatial resolution by selecting the maximum value of the four 2.5 km grid cells.

As stressed in the Introduction, owing to the hillslope-scale variation in the effective rainfall needed for triggering landslides, using multiple rainfall durations is crucial for elucidating relationships between spatial patterns of rainfall return levels and landslide density. Because the correct timing of respective landslide occurrence is unknown and probably different within each grid cell of the R/A precipitation dataset, the setting of a standardized rainfall period covering the rainfall for “cause” and “trigger” of landsliding is required for comparisons between spatial distributions of rainfall and landslides. In this study, the 72 h that accumulated the maximum rainfall during the examined rainfall event was used as the standardized rainfall period (P_{std}), as suggested by Tsunetaka. (2021). We assumed that the various landslides experienced in our study area occurred within this period. This assumption was based on the fact that the studied event brought unprecedented rainfall amount that outweighs the possible effects of antecedent rainfall on landslide occurrence (Marc et al., 2019; Guthrie and Evans, 2004). The temporal rainfall pattern was subsequently examined by computing the maximum rainfall intensity (rainfall intensity maxima) for multiple timespans (1, 2, 3, 6, 12, 24, 48, and 72 h) within the P_{std} .

To investigate the return levels (i.e., recurrence levels) of these rainfall intensity maxima, we developed the IDF curves that statistically fit the annual maxima series (AMS) of rainfall intensities observed over 1–72 h. We extracted the AMS from the 32-year (from 1988 to 2019) R/A precipitation dataset. Then, we used the Gumbel distribution, based on the L-moments method (Hosking, 1990), to fit the extracted AMS due to its few shape parameters that may reduce the estimation uncertainty (Frattini et al., 2009). Such a statistical model assumes an asymptotic behavior of the rainfall dataset. To assess the ability of the estimated distributions to represent the extracted AMS, we used the Kolmogorov-Smirnov (KS) test, which examines the goodness of fit between the estimated and observed cumulative distributions. Here, the null hypothesis assumes identical distributions. Therefore, the *p-value* calculated using an asymptotic distribution of the KS test statistic should be less than a significance level of 5 % to reject the null hypothesis.

2.3 Investigating rainfall controls on landslide spatial distribution

To investigate the spatial distribution of landslides over the landscape, we compared the spatial variation in landslide density among the grid cells of the R/A precipitation dataset. The landslide density is calculated as the number of landslides within a sliding window of about 25 km² (= R/A grid cell). These numbers are generally affected by the differences in topographic features (i.e., hills, mountains, plains, lakes) within the sliding window because landslides commonly occur in hilly and mountainous areas rather than plains (Lombardo et al., 2021). To avoid such a possible influence, we normalized the number of landslides within each sliding window by the area where the slope is higher than a threshold angle ($S_{threshold}$) assumed to be a minimum angle to allow landsliding. $S_{threshold}$ defines the threshold angle above which 90 % of landslides occurred (Prancevic et al., 2020) and was determined as 16.26° based on the DEM data



analysis (Fig. S1). To count the number of landslides in each grid cell, we first converted the polygons data of landslide scars to points locating the centroid of each polygon. Although medium and large landslides (landslides with area size exceeding the cutoff point of the FAD (439 m²)) counted only 28.12 % of the total landslides, their areas represented more than 70 % of the total landsliding area (i.e., the total scar areas of triggered landslides). Therefore, it is interesting to investigate rainfall controls on the density of both the total and only medium and large landslides. Accordingly, we computed two landslide density metrics, total landslide density (TD) and only medium and large landslide density (MLD), as the number of landslides per unit area (km²), for each grid cell using the following equations (1) and (2).

$$TD = \frac{\text{Total number of all landslides}}{\text{Area where Slope} > S_{\text{threshold}}} \quad (1)$$

$$MLD = \frac{\text{Number of medium and large landslides}}{\text{Area where Slope} > S_{\text{threshold}}} \quad (2)$$

By comparing rainfall return levels and landslide density metrics (i.e., TD and MLD), we intended to evaluate whether the number of total and relatively large landslides increases when rarely experienced rainfall intensities occur.

Our investigation started by evaluating the statistical correlation between calculated landslide density metrics (TD and MLD) and rainfall intensity maxima. We used Spearman's rank coefficient (ρ) to measure the non-parametric monotonicity of these relationships. Subsequently, we compared the variation in rainfall intensity maxima and their return levels and landslide density at the R/A grid cell scale beyond these statistical relationships. For a fair comparison, it is important to focus on R/A grid cells with a comparable distribution of hillslope angles $> S_{\text{threshold}}$ because landslide density in the R/A grid cells may depend on hillslope steepness (Prancevic et al., 2020). To this end, we first tested the differences in slope angles $> S_{\text{threshold}}$ within the examined grid cells using the Kruskal-Wallis static (Kruskal and Wallis, 1952). Then, we employed Dunn's post hoc test (Dunn, 1961) with a Bonferroni correction for the p -value for detecting the grid cells with similar mean rank sums of slopes (similar slope conditions). Here, the null hypothesis assumes no significant differences in the slope angles within the R/A grid cells. Therefore, the p -value should be higher than a significant level of 5 % to accept the null hypothesis (Dinno, 2017).

3 Results

3.1 Relationship between landslide density and rainfall intensity maxima

A line-shaped band of high rainfall intensity maxima matched the overall spatial pattern of triggered landslides (Fig. 3), which indicates that the spatial distribution of rainfall intensities constrains the landslide distribution. These maxima exhibited substantial differences at the grid cell scale, suggesting spatial disparity in the characteristics of the temporal rainfall pattern. The total triggered landslides were distributed within 23 R/A grid cells with a TD varied between 0.05 and 105.63 landslides/km² and an MLD ranging between 0.00 and 36.26 landslides/km² (Fig. 3). More than 65 % of total landslides occurred within only three R/A grid cells with a TD of 35.61, 103.88, and 105.63 landslides/km². The MLD



values in these grid cells were 11.98, 36.26, and 28.03 landslides/km², respectively, indicating the highest number of medium and large landslides occurred during the triggering event. From a statistical point of view, Spearman's rank correlation coefficients (Table 1) showed significant monotonic positive relationships between all computed maxima and TD (0.62 < ρ < 0.80) and MLD (0.68 < ρ < 0.84) at the 1 % level. Therefore, rainfall controls on landslide density cannot be explicitly grasped from a single rainfall intensity metric.

Focusing on three idealized pairs of grid cells with similar slope angles (P1, P2, and P3), as Dunn's test could not reject the null hypothesis (Table S1), we investigated the relation between rainfall intensity maxima and landslide density over the paired grid cells (Fig. 4). Despite the similarity in slope angles, the differences in landslide density (TD and MLD) between the paired grid cells in P1 and P2 were well distinguishable, which makes them ideal candidates for evaluating the controls of rainfall intensity maxima on landslide density. On the other hand, these differences were less pronounced over the grid cells in P3.

In P1, the rainfall intensity maxima observed over the grid cell that experienced high landslide density (TD = 35.61 and MLD = 11.98 landslides/km²) were 1.5 to 1.7 times higher than those observed in the low landslide density grid cell (Fig. 4a). Similarly, the differences in rainfall intensity maxima over the paired grid cells in P2 varied between 1.7 to 3.3 times of rainfall intensity (Fig. 4b). We further noted that in P3, rainfall maxima recorded for 12–72 h over the two grid cells (Fig. 4c) were comparable. Unlikely, the grid cell with higher landslide density (TD = 20.91 and MLD = 5.65 landslides/km²) experienced a little higher rainfall intensity for 1–6 h rainfall timespans (\approx 1.15 times). This means that a little higher rainfall intensity at short timespans may cause a relative increase in landslide density (\approx 3.5 times for TD). However, this increase was substantial when rainfall intensity maxima were much higher at all examined timespans within the P_{std} . Indeed, the differences in TD between the paired grid cells in P1 and P2 reached \approx 700 times and \approx 70 times, respectively. We further noted that irrespectively of the differences in slope angles, the low landslide density grid cells in P3 shared comparable rainfall intensity maxima for 1–3 h timespans with the low landslide density grid cells in P1 (Fig. 4a-c) but relatively higher 6–72 rainfall intensity maxima (\approx 1.25 times). Nonetheless, the difference in landslide density between the two grid cells was high (\approx 110 times for TD).

Observing the other grid cells with landslides except three where most landslides occurred in areas affected by anthropogenic activities (e.g., slopes surrounding cropland and paddy field), we found that the observations over the three idealized pairs were also valid for most grid cells (Fig. S2). Indeed, we noticed a spatial disparity in rainfall intensity maxima that hamper distinguishing thresholds for the temporal rainfall pattern characteristics, which explain the differences in landslide density. Therefore, analyzing the potential relation between the spatial patterns of rainfall return levels and landslide density is needed.

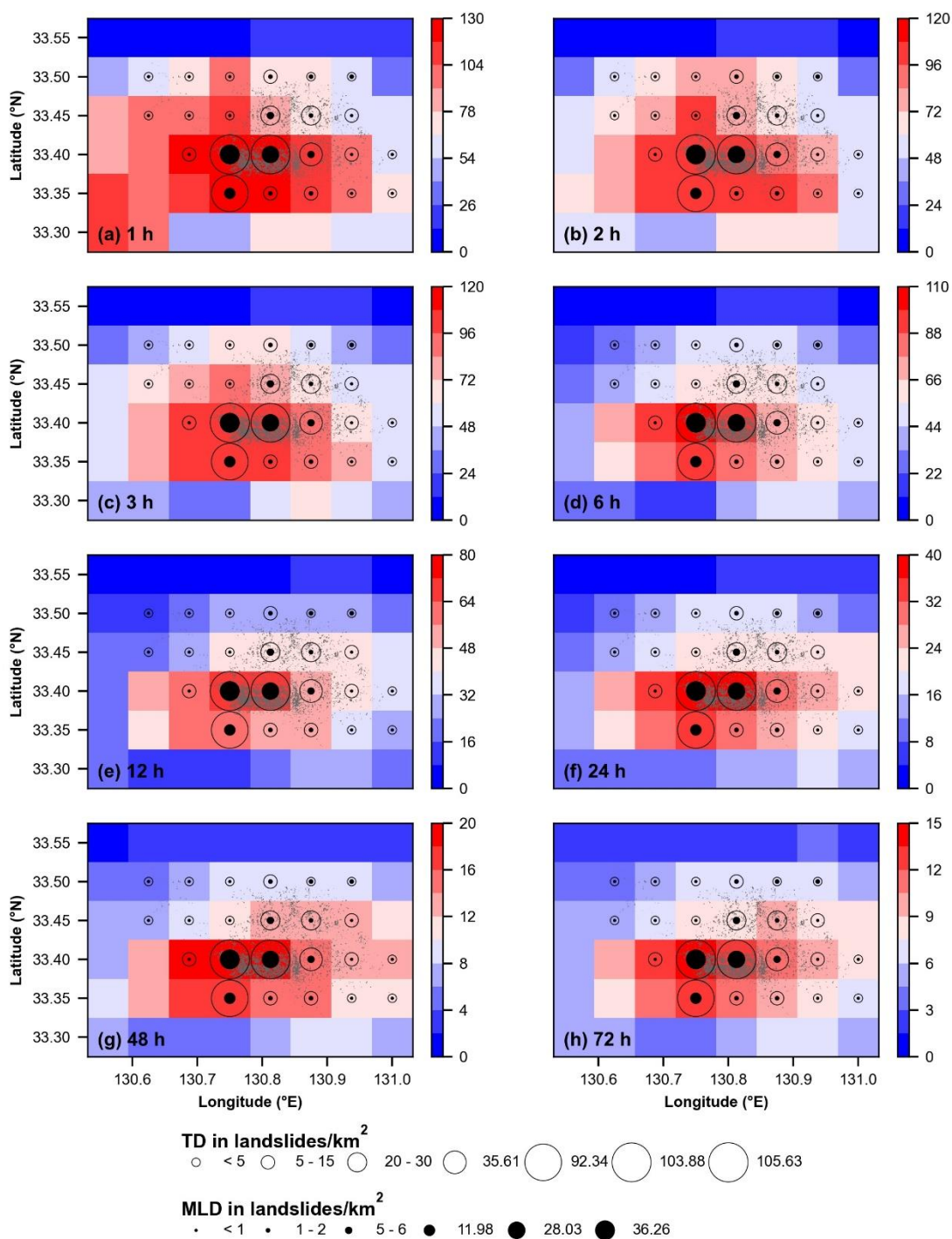


Figure 3: Spatial distribution maps of rainfall intensity maxima for 1 to 72 h timespans within the P_{std} in mm/h, triggered landslides (grey polygons), and landslide density metrics (circles)



225 **Table 1: Spearman rank correlation between rainfall intensity maxima and landslide density metrics**

Rainfall timespan (h)	1	2	3	6	12	24	48	72
ρ (TD)	0.62*	0.66*	0.74*	0.79*	0.79*	0.79*	0.79*	0.80*
ρ (MLD)	0.68*	0.71*	0.77*	0.84*	0.82*	0.81*	0.81*	0.82*

* significant at 1 % level

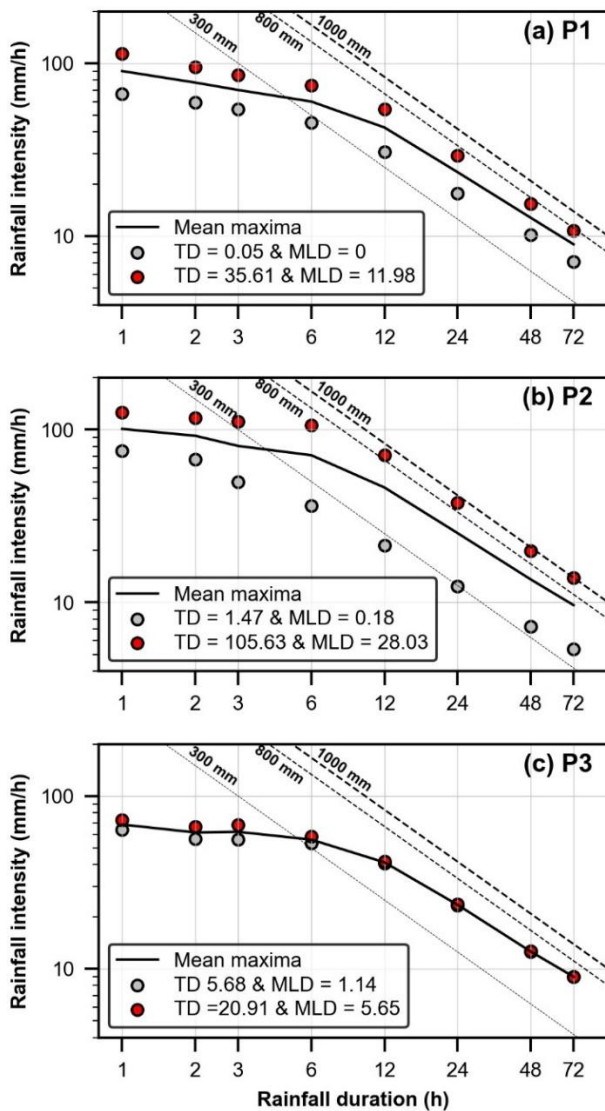


Figure 4: Comparison of rainfall intensity maxima over grid cell pairs with similar slope angles. Dashed lines correspond to theoretical rainfall totals of 300, 800, and 1000 mm.



230 3.2 Return levels of rainfall intensity maxima

The Gumbel distributions estimating rainfall return levels were able to represent the AMS of rainfall intensity for 1–72 timespans, as the K-S test could not reject the null hypothesis (p -value > 0.05) (Fig. S3). Rainfall intensity maxima estimated for various return periods (5–100 years) and durations (1–72 h) displayed substantial spatial differences at the grid cell scale (Figs. S4–S8). For instance, the 100-year return level of 24-h rainfall intensity maxima varied between 16
235 and 28 mm/h (Fig. S8f), indicating different IDF curves at the grid cell scale. Thus, evaluating the return levels of computed rainfall intensity maxima at the grid cell scale can be effective in setting a quantitative reference for spatial rainfall analysis.

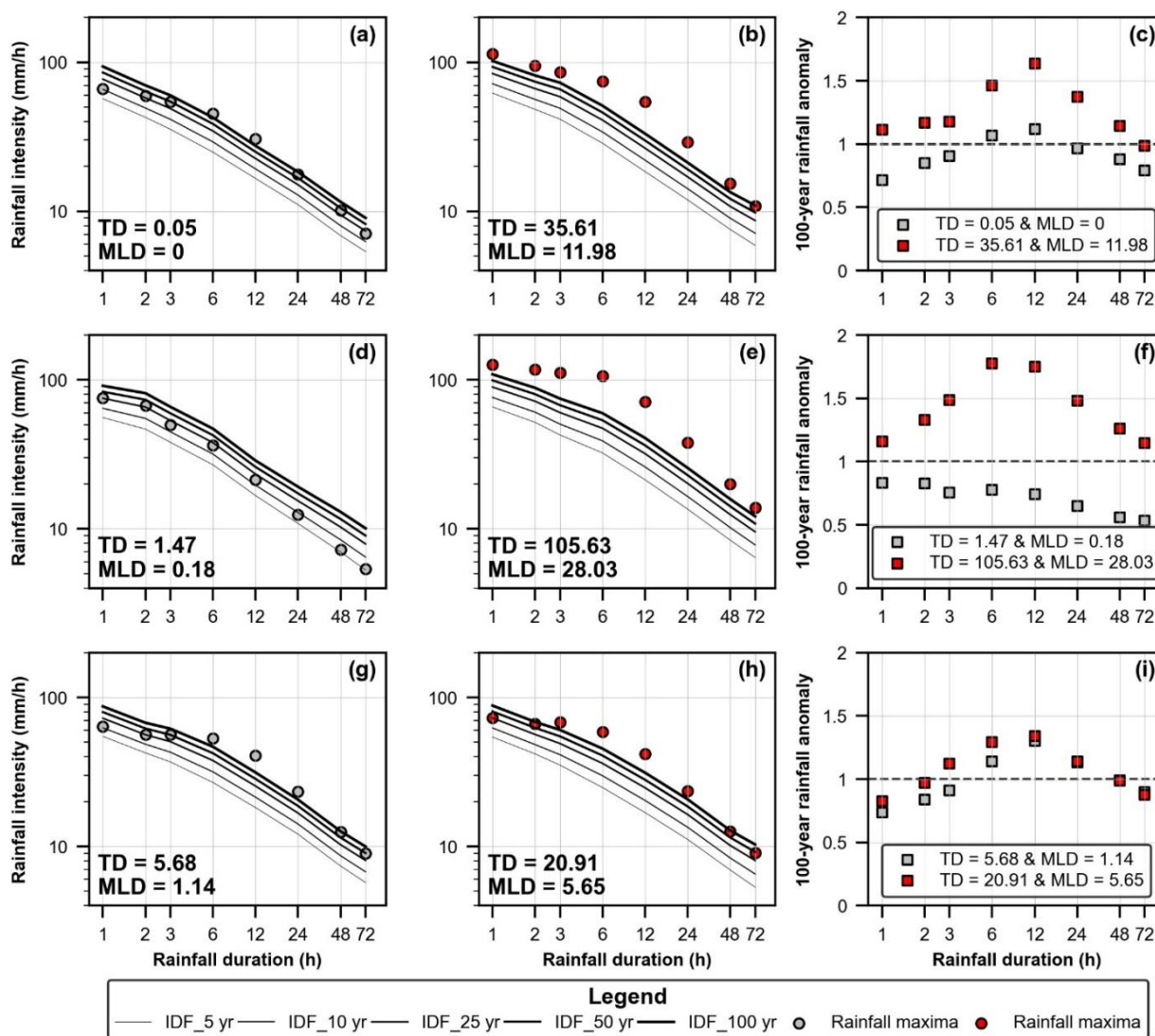
Comparing the position of rainfall intensity maxima in the IDF curves discloses disparate return levels (Figs. 5 and S9). These differences were clear for the paired grid cells with similar slope angle conditions (Fig. 5). The return levels of all
240 rainfall intensity maxima over the high landslide density grid cells in P1 and P2 (Fig 5 b and c) exceeded or hit the IDF curve for the 100-year return period, mirroring unprecedented and extreme rainfall intensities. Accordingly, the ratio between the rainfall intensity maxima within the P_{std} and the estimated rainfall intensity for a 100-year return period referred to hereafter as “100-year rainfall anomaly”, exceeded one at all timespans (Fig 5 c and f). On the other hand, the 100-year rainfall anomaly exceeded one only at 6 and 12 h rainfall timespans for the low landslide density grid cell in P1
245 (Fig 5c). It was lower than one at all timespans for the low landslide density grid cell in P2 (Fig 5f), meaning that rainfall intensities did not reach a return level of the 100-year order (Fig 5d). Therefore, the number of triggered landslides increased substantially (≈ 70 to ≈ 700 times in terms of TD) when rainfall return levels exceeded the 100-year return period in the IDF curves for the multiple examined timespans (i.e., 1–72 h).

Focusing on the grid cells in P3 (Fig. 5g and h), we noted disparate return levels for 1–6 h-intensities, although the
250 similarities in return levels of rainfall intensity maxima for 12–72 h. This led to a comparable 100-year rainfall anomaly for 12–72 h rainfall durations. However, the 100-year rainfall anomaly for 1–6 h periods was slightly higher in the high landslide density grid cell (Fig 5i), particularly for the 3-h rainfall duration, which exceeded one in the case of the high landslide density grid cell (TD = 20.91 and MLD = 5.65 landslides/km²). This means that the disparities in rainfall return levels could be the cause for the relative difference in landslide density between the two paired grid cells. Interestingly,
255 irrespective of the variation in slope angle values and comparable rainfall conditions between the low landslide density grid cells in P1 (Fig. 5a) and P3 (Fig. 5g), the comparison of the 100-year rainfall anomaly could explain the substantial difference in landslide density between the two grid cells (≈ 110 times for TD). Indeed, the 100-year rainfall anomaly was higher in the low landslide-density grid cell in P3 (Fig. 5i) than in the low landslide-density grid cell in P1 (Fig. 5c), meaning that rainfall intensities experienced over the former were more extreme than those experienced over the latter.

260 Overall, rainfall intensity maxima over grid cells with high landslide density exhibited higher return levels than those over lower landslide density (Fig. S9). Irrespective of the differences in slope angle distribution, we can categorize the



grid cells that experienced landslides based on differences in the 100-year rainfall anomaly and landslide density. Accordingly, we found that over the high landslide density grid cells ($TD > 30$ and $MLD > 10$ landslides/km²), of which the grid cells with high landslide density in P1 and P2, the 100-year rainfall anomaly exceeded one at all timespans (Fig S10b). In other words, rainfall intensities for all examined timespans (i.e., 1–72 h) exhibited return levels exceeding the 100-year return period. While over low landslide density grid cells ($TD < 30$ and $MLD < 10$ landslides/km²), which include the grid cells with low landslide density in P1 and P2 and the two paired grid cells in P3, the 100-year rainfall anomaly was generally lower than one or exceeded one only at some timespans within the P_{std} (Fig S10a).



270 **Figure 5: Return levels of rainfall intensity maxima for multiple timespans (1–72 h) within the P_{std} in the IDF curves (a, b, d, e, g, h) and comparisons of the 100-year rainfall anomaly (c, f, i) over the paired grid cells in P1, P2, and P3**



4 Discussion

Our results demonstrate that landslide density in terms of TD and MLD varied depending on rainfall return levels for the examined timespans ranging from 1 to 72 h, which characterize the spatiotemporal rainfall pattern of the triggering rainfall event.

When rainfall exhibited return levels exceeding the 100-year return period for the various timespans from 1 to 72 hours (e.g., Fig. 5b, e), the number of total landsliding was substantially high ($TD > 30$ landslides/km²). The high landslide density can dictate that the rare and extreme rainfall intensities for multiple timespans from 1 to 72 h could satisfy the trigger and dynamic predisposition factors for landsliding of numerous hillslopes. The constraint of these unprecedented rainfall intensities on landslide density overwhelmed that of topographic conditions (Fig 5), as we observed substantial landslide density differences over grid cells with comparable slope angles. This accentuates the importance of high rainfall return levels in inducing widespread landslides (Iida, 2004; Griffiths et al., 2009; Segoni et al., 2014). In parallel, the density of large and medium landslides was also the highest ($MLD > 10$ landslides/km²) during the examined rainfall event. This implies that the high rainfall return levels for the various examined timespans constrain the occurrence of relatively large landslides and suggests that the spatiotemporal rainfall pattern characteristics can also govern the landslide size distribution, which is consistent with the findings of Marc et al. (2018). In contrast, when rainfall return levels did reach the 100-year return period only at specific timespans, lower landslide density ($TD < 30$ and $MLD < 10$ landslides/km²) was observed (e.g., Fig. 5a, g, h). In other words, only some periods of rainfall (e.g., 6–48 h) exhibited extreme and rarely experienced intensities over the grid cells, resulting in the failure of only the relatively vulnerable hillslopes. In any case, we can conclude that whether rainfall intensities reach high return levels in a wide timespan, ranging from a few hours to several days, is one of the key determinants of the density of total landsliding and relatively large landslides.

From a statistical perspective, the significant quantitative correlations between rainfall intensity maxima and landslide density (TD and MLD) suggest an increased landslide density with increased rainfall intensities for the various examined timespans (i.e., 1–72 h) (Table 1). These statistical relationships are not surprising since they are likely arising from the correlations between the different rainfall intensity maxima (Table S2). However, this does not necessarily mean that landslide density increases with increased specific-duration rainfall intensity (e.g., rainfall intensity maxima for 6 h). Indeed, our results showed substantial differences in landslide density over grid cells with comparable short-duration rainfall intensity maxima but disparate long-duration rainfall intensities (e.g., low landslide-density grid cells in P1 and P3, Fig. 4a, c). The pronounced difference in landslide density is likely due to the disparity in rainfall characteristics that affected the slope stability differently, initiating a disparate number of landslides. Thus, although the quantitative correlations in Table 1 can successfully predict landslide density, as indicated by Chang et al. (2008) and Dai and Lee.



(2001), relying on a single rainfall metric (e.g., 6 h rainfall intensity maxima) may lead to spurious interpretations regarding rainfall controls on landslide density due to concealing the characteristics of the temporal rainfall pattern.

305 Regardless of the spatial variation in rainfall intensity maxima characterizing the temporal rainfall pattern, the return levels could evaluate the exceptionality and extremity of rainfall for various timespans. Indeed, by comparing the rainfall return levels over two grid cells, it was clear that the grid cells with the highest landslide density experienced higher rainfall return levels for the various timespans (e.g., Fig. 5 c, f, a vs. g). This can dictate that rainfall with higher return levels was more extreme and less frequent, having a higher potential to cause numerous landslides over the landscape.

310 Accordingly, the differences in rainfall return levels could explain the substantial spatial disparity in landslide density. Thus, the comparison of rainfall return levels can be a valid approach for understanding the substantial differences in landslide density regardless of the variation in temporal rainfall pattern characteristics.

Given the relatively homogenous regolith of the study area this research focused on, landslide spatial distribution was likely governed by only rainfall return levels. However, other landslide susceptibility factors may intervene if the studied

315 rainfall event is experienced in a heterogenous regolith. In this context, Crozier (2017) proposed a storm cell model that links landslide density to rainfall intensity, impact magnitude, and the criticality of landslide susceptibility parameters to examine rainfall controls on landslide spatial distribution during large-scale rainfall events. The proposed model assumes the occurrence of landslides in a circular pattern mirroring rainfall intensity during rainfall events and defines three landslide response zones: the core (storm center), the middle, and the periphery zone. In analogy to the storm cell model

320 of Crozier (2017), which suggests an overwhelm of the influence of extremely intense rainfall in the core zone, where total rainfall > 500 mm, on other landslide susceptibility factors, the high rainfall return levels experienced over high landslide density grid cells may outweigh the influence of terrain-related parameters if experienced in other sites with heterogenous regolith settings. Therefore, when rainfall intensities reach high return levels for a wide timespan ranging from an hour to a few days, high landslide density over the landscape can be expected regardless of variations in terrain

325 characteristics (land use, lithology, and topography). In contrast, when rainfall return intensities exceed the 100-year return level only for specific timespans (e.g., 6–48 h), the variation in landslide susceptibility factors can also govern landslide density. This can be supported in analogy to the findings of Crozier (2017) in the middle zone of the proposed storm model.

Last, it is worth noting that landslides occurred even when rainfall did not reach the 100-year return level at any of the

330 examined timespans (Fig S9 b, e, f). However, landslide density over these grid cells (i.e., grid cells where rainfall did not reach the 100-year return level) was considerably low ($\approx 0.4\text{--}1.5$ landslide/km² in terms of TD) compared with most other grid cells. Landslide occurrence over these grid cells during the examined rainfall event could be constrained by terrain settings (e.g., land cover) as the rainfall return levels were low. Also, it could likely arise from a misinterpretation of the orthophotos used for preparing the landslide inventory. Therefore, landslides can occur even if rainfall return levels



335 do not reach the 100-year return but with substantially low density. In any case, comparing rainfall return levels in the
IDF curves can explain the substantial differences in landslide density due to considering multiple return periods.

5 Conclusions

This study explored the spatiotemporal pattern of an extreme rainfall event that triggered widespread landslides to reveal
what rainfall characteristics control the spatial landslide distribution. We examined the temporal rainfall pattern by
340 computing the maximum rainfall intensity for multiple timespans (1–72 h) within a 72-h duration that accumulated the
maximum rainfall amount (P_{std}) during the examined rainfall event. Landslide density, in terms of the total number of
triggered landslides (TD) and only medium and large landslides (MLD), significantly correlated with all computed
rainfall intensity maxima. However, this did not necessarily mean that landslide density increases with increased rainfall
intensity maxima for a specific time span. More than 65 % of triggered landslides occurred in areas where all computed
345 rainfall intensity maxima exceeded or hit the 100-year return levels, with a high density ($TD > 30$ landslides/km² and
 $MLD > 10$ landslides/km²). This corresponds to a 100-year rainfall anomaly, which calculates the ratio between rainfall
intensity maxima and estimated intensity for the 100-year return period, exceeding one at all timespans within the P_{std} .
On the other hand, lower landslide density was found in areas of rainfall characterized by intensities that did not or did
reach the 100-year return period only at some timespans within the P_{std} (e.g., 6–48 h). The constraint of rainfall return
350 levels on landslide density overwhelmed that of topographic conditions, as we observed substantially different landslide
densities in areas with similar slope angles but different rainfall return levels. Overall, this work reveals the role played
by the spatial patterns of rainfall return levels for various timespans in controlling landslide density. It further suggests
that whether rainfall intensities reach high return levels for a wide timespan, ranging from a few hours to several days, is
one of the key determinants of the density of total landsliding and relatively large landslides.

355 Code availability

The multidimensional analysis carried out in this paper used python open-source libraries: “rasterio” (Gillies and Others,
2013), “xarray” (Hoyer et al., 2021), “rioxarray” (Snow et al., 2021), and “xclim” (Logan et al., 2021). All figures were
created using the python open-source library Matplotlib (Caswell et al., 2021).

Data availability

360 The landslide inventory data is available upon agreement by the Ministry of Land, Infrastructure, Transport, and Tourism
of Japan (<http://www.qsr.mlit.go.jp/>), which holds the data copyright. The radars-driven precipitation data is a



commercial product of the Japan Meteorological Agency and can be purchased from the Japan Meteorological Business Support Center (<http://www.jmbasc.or.jp/jp/>). The DEM data used in this research can be freely downloaded from the GSI website (<https://fgd.gsi.go.jp/download/menu.php>).

365 **Competing interests**

The contact author has declared that none of the authors has any competing interests.

Acknowledgements

We acknowledge the Geospatial Information Authority of Japan (GSI) for freely providing the DEM data.

Financial support

370 This work was supported by the project “Development of Technology for Impacts, Mitigation and Adaptation to Climate Change in The Sectors of Agriculture, Forestry and Fisheries” of the Agriculture, Forestry, and Fisheries Research Council (Japan).

Author contributions

SM designed the study, performed the analyses, and wrote the paper. HT performed the FAD analysis and reviewed the
375 paper.

References

- Abancó, C., Bennett, G., Matthews, A., Matera, M., and Tan, F.: The role of geomorphology, rainfall and soil moisture in the occurrence of landslides triggered by 2018 Typhoon Mangkhut in the Philippines, *Nat. Hazards Earth Syst. Sci.*, 1–32, <https://doi.org/10.5194/nhess-2020-259>, 2020.
- 380 Benda, L. and Dunne, T.: Stochastic forcing of sediment supply to channel networks from landsliding and debris flow, *Water Resour. Res.*, 33, 2849–2863, <https://doi.org/10.1029/97WR02388>, 1997.
- Berti, M., Martina, M. L. V., Franceschini, S., Pignone, S., Simoni, A., and Pizziolo, M.: Probabilistic rainfall thresholds for landslide occurrence using a Bayesian approach, 117, 1–20, <https://doi.org/10.1029/2012JF002367>, 2012.
- Bogaard, T. and Greco, R.: Invited perspectives: Hydrological perspectives on precipitation intensity-duration thresholds
385 for landslide initiation: Proposing hydro-meteorological thresholds, *Nat. Hazards Earth Syst. Sci.*, 18, 31–39,



<https://doi.org/10.5194/nhess-18-31-2018>, 2018.

Büschelberger, M., Wilk, J., Hergarten, S., and Preusser, F.: Size–frequency distribution of shallow landslides in the Black Forest, Germany, *Earth Surf. Process. Landforms*, 47, 179–192, <https://doi.org/10.1002/esp.5237>, 2022.

Caswell, Thomas A., Michael Droettboom, Lee, A., Andrade, E. S. de, Hoffmann, T., Hunter, J., Klymak, J., Firing, E., Stansby, D., Varoquaux, N., Nielsen, J. H., Root, B., May, R., Elson, P., Seppänen, J. K., Dale, D., Lee, J.-J., McDougall, D., Straw, A., Hobson, P., Hannah, Gohlke, C., Vincent, A. F., Yu, T. S., Ma, E., Silvester, S., Moad, C., Kniazev, N., Ernest, E., and Ivanov, P.: *matplotlib/matplotlib: REL: v3.5.0*, <https://doi.org/10.5281/zenodo.5706396>, 2021.

Chang, K. T., Chiang, S. H., and Lei, F.: Analysing the Relationship Between Typhoon- Triggered Landslides and Critical Rainfall Conditions, *Earth Surf. Process. Landforms*, 33, 1261–1271, <https://doi.org/10.1002/esp>, 2008.

395 Chen, Y. C., Chang, K. T., Chiu, Y. J., Lau, S. M., and Lee, H. Y.: Quantifying rainfall controls on catchment-scale landslide erosion in Taiwan, *Earth Surf. Process. Landforms*, 38, 372–382, <https://doi.org/10.1002/esp.3284>, 2013.

Chigira, M., Sixian, L., and Matsushi, Y.: Landslide disaster induced by the 2017 northern Kyushu rainstorm, *Disaster Prevention Research Institute Annals*, 28-35 (in Japanese, with English abstract) pp., 2018.

Clauset, A., Shalizi, C. R., and Newman, M. E. J.: Power-law distributions in empirical data, *SIAM Rev.*, 51, 661–703, <https://doi.org/10.1137/070710111>, 2009.

Crozier, M. J.: A proposed cell model for multiple-occurrence regional landslide events: Implications for landslide susceptibility mapping, *Geomorphology*, 295, 480–488, <https://doi.org/10.1016/j.geomorph.2017.07.032>, 2017.

Dai, F. C. and Lee, C. F.: Frequency-volume relation and prediction of rainfall-induced landslides, *Eng. Geol.*, 59, 253–266, [https://doi.org/https://doi.org/10.1016/S0013-7952\(00\)00077-6](https://doi.org/https://doi.org/10.1016/S0013-7952(00)00077-6), 2001.

405 Dinno, A.: Package ‘dunn.test,’ CRAN Repos., 1–7, 2017.

Dunn, O. J.: Multiple Comparisons among Means, *J. Am. Stat. Assoc.*, 56, 52–64, <https://doi.org/10.1080/01621459.1961.10482090>, 1961.

Emberson, R., Kirschbaum, D. B., Amatya, P., Tanyas, H., and Marc, O.: Insights from the topographic characteristics of a large global catalog of rainfall-induced landslide event inventories, *Nat. Hazards Earth Syst. Sci.*, 22, 1129–1149, <https://doi.org/10.5194/nhess-22-1129-2022>, 2022.

Frattoni, P. and Crosta, G. B.: The role of material properties and landscape morphology on landslide size distributions, *Earth Planet. Sci. Lett.*, 361, 310–319, <https://doi.org/10.1016/j.epsl.2012.10.029>, 2013.

Frattoni, P., Crosta, G., and Sosio, R.: Approaches for defining thresholds and return periods for rainfall-triggered shallow landslides, *Hydrol. Process.*, 23, 1444–1460, <https://doi.org/10.1002/hyp.7269>, 2009.

415 Froude, M. J. and Petley, D. N.: Global fatal landslide occurrence from 2004 to 2016, *Nat. Hazards Earth Syst. Sci.*, 18, 2161–2181, <https://doi.org/10.5194/nhess-18-2161-2018>, 2018.

Gao, L., Zhang, L. M., and Cheung, R. W. M.: Relationships between natural terrain landslide magnitudes and triggering rainfall based on a large landslide inventory in Hong Kong, *Landslides*, 15, 727–740, <https://doi.org/10.1007/s10346->



- 017-0904-x, 2018.
- 420 Gillies, S. and Others: Rasterio: geospatial raster I/O for Python programmers, <https://github.com/mapbox/rasterio>, 2013.
- Griffiths, P. G., Magirl, C. S., Webb, R. H., Pytlak, E., Troch, P. A., and Lyon, S. W.: Spatial distribution and frequency of precipitation during an extreme event: July 2006 mesoscale convective complexes and floods in southeastern Arizona, *Water Resour. Res.*, 45, 1–14, <https://doi.org/10.1029/2008WR007380>, 2009.
- Guthrie, R. H. and Evans, S. G.: Magnitude and frequency of landslides triggered by a storm event, Loughborough Inlet, British Columbia, *Nat. Hazards Earth Syst. Sci.*, 4, 475–483, <https://doi.org/10.5194/nhess-4-475-2004>, 2004.
- 425 Guzzetti, F., Malamud, B. D., Turcotte, D. L., and Reichenbach, P.: Power-law correlations of landslide areas in central Italy Power-law correlations of landslide areas in central Italy, *Earth Planet. Sci. Lett.*, 195, 169–183, [https://doi.org/10.1016/S0012-821X\(01\)00589-1](https://doi.org/10.1016/S0012-821X(01)00589-1), 2002.
- Guzzetti, F., Cardinali, M., Reichenbach, P., Cipolla, F., Sebastiani, C., Galli, M., and Salvati, P.: Landslides triggered by the 23 November 2000 rainfall event in the Imperia Province, Western Liguria, Italy, *Eng. Geol.*, 73, 229–245, <https://doi.org/10.1016/j.enggeo.2004.01.006>, 2004.
- Hirockawa, Y., Kato, T., Tsuguti, H., and Seino, N.: Identification and classification of heavy rainfall areas and their characteristic features in Japan, *J. Meteorol. Soc. Japan*, 98, 835–857, <https://doi.org/10.2151/jmsj.2020-043>, 2020.
- Hosking, J. R. .: L-moments: Analysis and estimation of distributions using linear combination of order statistics, *J. R. Stat. Soc. Ser. B*, 52, 105–124, <https://doi.org/10.1111/j.2517-6161.1990.tb01775.x>, 1990.
- 435 Hovius, N., Stark, C. P., and Allen, P. A.: Sediment flux from a mountain belt derived by landslide mapping, *Geology*, 25, 231–234, [https://doi.org/10.1130/0091-7613\(1997\)025<0231:SFFAMB>2.3.CO;2](https://doi.org/10.1130/0091-7613(1997)025<0231:SFFAMB>2.3.CO;2), 1997.
- Hoyer, S., Roos, M., Hamman, J., Deepak Cherian, K., Fitzgerald, C., Hauser, M., Fujii, K., Maussion, F., and Al, E.: `pydata/xarray: v0.20.1`, <https://doi.org/10.5281/zenodo.5648431>, 2021.
- 440 Iida, T.: A stochastic hydro-geomorphological model for shallow landsliding due to rainstorm, *Catena*, 34, 293–313, [https://doi.org/10.1016/S0341-8162\(98\)00093-9](https://doi.org/10.1016/S0341-8162(98)00093-9), 1999.
- Iida, T.: Theoretical research on the relationship between return period of rainfall and shallow landslides, *Hydrol. Process.*, 18, 739–756, <https://doi.org/10.1002/hyp.1264>, 2004.
- Iverson, M.: Landslide triggering by rain infiltration, *Water Resour. Res.*, 36, 1897–1910, 2000.
- 445 Jones, J. N., Boulton, S. J., Stokes, M., Bennett, G. L., and Whitworth, M. R. Z.: 30-year record of Himalaya mass-wasting reveals landscape perturbations by extreme events, *Nat. Commun.*, 12, 1–16, <https://doi.org/10.1038/s41467-021-26964-8>, 2021.
- Ko, F. W. Y. and Lo, F. L. C.: Rainfall-based landslide susceptibility analysis for natural terrain in Hong Kong - A direct stock-taking approach, *Eng. Geol.*, 215, 95–107, <https://doi.org/10.1016/j.enggeo.2016.11.001>, 2016.
- 450 Korup, O., Densmore, A. L., and Schlunegger, F.: The role of landslides in mountain range evolution, *Geomorphology*, 120, 77–90, <https://doi.org/10.1016/j.geomorph.2009.09.017>, 2010.



- Kruskal, W. H. and Wallis, W. A.: Use of Ranks in One-Criterion Variance Analysis, *J. Am. Stat. Assoc.*, 47, 583–621, <https://doi.org/10.1080/01621459.1952.10483441>, 1952.
- Lanni, C., Borga, M., Rigon, R., and Tarolli, P.: Modelling catchment-scale shallow landslide occurrence by means of a subsurface flow path connectivity index, *Hydrol. Earth Syst. Sci.*, 16, 3959–3971, <https://doi.org/10.5194/hessd-9-4101-2012>, 2012.
- Lehmann, P. and Or, D.: Hydromechanical triggering of landslides: From progressive local failures to mass release, *Water Resour. Res.*, 48, 1–24, <https://doi.org/10.1029/2011WR010947>, 2012.
- Logan, T., Bourgault, P., Smith, Trevor James Huard, D., Biner, S., Labonté, M.-P., Rondeau-Genesse, G., Fyke, J., Aoun, A., Roy, P., Ehbrecht, C., Caron, D., Stephens, A., Whelan, C., Low, J.-F., and Lavoie, J.: Ouranosinc/xclim: v0.31.0, <https://doi.org/10.5281/zenodo.5649661>, 2021.
- Lombardo, L., Tanyas, H., Huser, R., Guzzetti, F., and Castro-Camilo, D.: Landslide size matters: A new data-driven, spatial prototype, *Eng. Geol.*, 293, <https://doi.org/10.1016/j.enggeo.2021.106288>, 2021.
- Makihara, Y.: Algorithms for precipitation nowcasting focused on detailed analysis using radar and raingauge data, Technical Reports of the Meteorological Research Institute, 63–111 pp., 2000.
- Malamud, B. D., Turcotte, D. L., Guzzetti, F., and Reichenbach, P.: Landslide inventories and their statistical properties, *Earth Surf. Process. Landforms*, 29, 687–711, <https://doi.org/10.1002/esp.1064>, 2004.
- Marc, O., Stumpf, A., Malet, J. P., Gosset, M., Uchida, T., and Chiang, S. H.: Initial insights from a global database of rainfall-induced landslide inventories: The weak influence of slope and strong influence of total storm rainfall, *Earth Surf. Dyn.*, 6, 903–922, <https://doi.org/10.5194/esurf-6-903-2018>, 2018.
- Marc, O., Gosset, M., Saito, H., Uchida, T., and Malet, J. P.: Spatial Patterns of Storm-Induced Landslides and Their Relation to Rainfall Anomaly Maps, *Geophys. Res. Lett.*, 46, 11167–11177, <https://doi.org/10.1029/2019GL083173>, 2019.
- Medwedeff, W. G., Clark, M. K., Zekkos, D., and West, A. J.: Characteristic landslide distributions: An investigation of landscape controls on landslide size, *Earth Planet. Sci. Lett.*, 539, <https://doi.org/10.1016/j.epsl.2020.116203>, 2020.
- Milledge, D. G., Bellugi, D., Mckean, J. A., Densmore, A. L., and Dietrich, W. E.: A multidimensional stability model for predicting shallow landslide size and shape across landscapes David, J. *Geophys. Res. Earth Surf.*, 119, 2481–2504, <https://doi.org/doi:10.1002/2014JF003135>, 2014.
- Mtibia, S. and Asano, S.: Hydrological evaluation of radar and satellite gauge-merged precipitation datasets using the SWAT model: Case of the Terauchi catchment in Japan, *J. Hydrol. Reg. Stud.*, 42, 101134, <https://doi.org/10.1016/j.ejrh.2022.101134>, 2022.
- Nagata, K.: Quantitative Precipitation Estimation and Quantitative Precipitation Forecasting by the Japan Meteorological Agency, RSMC Tokyo–Typhoon Center Technical Review, 37–50 pp., <https://doi.org/Online> at: <http://www.jma.go.jp/jma/eng/jma-center/rsmc-hp-pub-eg/techrev/text13-2.pdf>, 2011.



- 485 Nagata, K. and Tsujimura, Y.: Characteristics of radar/raingaugeanalyzed precipitation and short-range precipitation forecast along with notices on their usage, 9-4 (in Japanese) pp., 2006.
- Prancevic, J. P., Lamb, M. P., McArdeell, B. W., Rickli, C., and Kirchner, J. W.: Decreasing Landslide Erosion on Steeper Slopes in Soil-Mantled Landscapes, *Geophys. Res. Lett.*, 47, 1–9, <https://doi.org/10.1029/2020GL087505>, 2020.
- Segoni, S., Rossi, G., Rosi, A., and Catani, F.: Computers & Geosciences Landslides triggered by rainfall: A semi-
490 automated procedure to define consistent intensity – duration thresholds, *Comput. Geosci.*, 63, 123–131, <https://doi.org/10.1016/j.cageo.2013.10.009>, 2014.
- Segoni, S., Battistini, A., Rossi, G., Rosi, A., Lagomarsino, D., Catani, F., Moretti, S., and Casagli, N.: Technical Note: An operational landslide early warning system at regional scale based on space-time-variable rainfall thresholds, *Nat. Hazards Earth Syst. Sci.*, 15, 853–861, <https://doi.org/10.5194/nhess-15-853-2015>, 2015.
- 495 Sidle, R. C. and Bogaard, T. A.: Dynamic earth system and ecological controls of rainfall-initiated landslides, *Earth-Science Rev.*, 159, 275–291, <https://doi.org/10.1016/j.earscirev.2016.05.013>, 2016.
- Snow, A. D., Brochart, D., Bell, R., Chegini, T., Amici, A., Annex, A., Hoeser, D., Bunt, F., Hamman, J., Zehner, M., Henderson, S., Miller, S., Badger, T. G., Augspurger, T., Braun, R., Miller, S., and Snow, A. D.: *corteva/rioxarray: 0.9.0* Release, <https://doi.org/10.5281/zenodo.5724719>, 2021.
- 500 Stark, C. P. and Hovius, N.: The characterization of landslide size distributions, *Geophys. Res. Lett.*, 28, 1091–1094, <https://doi.org/https://doi.org/10.1029/2000GL008527>, 2001.
- Tanyaş, H., van Westen, C. J., Allstadt, K. E., and Jibson, R. W.: Factors controlling landslide frequency–area distributions, *Earth Surf. Process. Landforms*, 44, 900–917, <https://doi.org/10.1002/esp.4543>, 2019.
- Tsunetaka, H.: Comparison of the return period for landslide-triggering rainfall events in Japan based on standardization
505 of the rainfall period, *Earth Surf. Process. Landforms*, 46, 2984–2998, <https://doi.org/10.1002/esp.5228>, 2021.
- Urita, S., Saito, H., and Matsuyama, H.: Temporal and Spatial Discontinuity of Radar/Raingauge-Analyzed Precipitation That Appeared in Relation to the Modification of Its Spatial Resolution, *Hydrol. Res. Lett.*, 5, 37–41, <https://doi.org/10.3178/hrl.5.37>, 2011.
- Wu, W. and Sidle, R.: A distributed slope stability model for steep forested basins, *Water Resour. Res.*, 31, 2097–2110,
510 <https://doi.org/doi.org/10.1029/95WR01136>, 1995.
- Yamada, M., Matsushi, Y., Chigira, M., and Mori, J.: Seismic recordings of landslides caused by Typhoon Talas (2011), Japan, *Geophys. Res. Lett.*, 39, 1–5, <https://doi.org/10.1029/2012GL052174>, 2012.
- Yano, A., Shinohara, Y., Tsunetaka, H., Mizuno, H., and Kubota, T.: Distribution of landslides caused by heavy rainfall events and an earthquake in northern Aso Volcano, Japan from 1955 to 2016, *Geomorphology*, 327, 533–541,
515 <https://doi.org/10.1016/j.geomorph.2018.11.024>, 2019.